SOFT ROBOTICS Volume 00, Number 00, 2023 © Mary Ann Liebert, Inc. DOI: 10.1089/soro.2021.0173



Open camera or QR reader and scan code to access this article and other resources online.



Tunable, Textile-Based Joint Impedance Module for Soft Robotic Applications

Ciarán T. O'Neill, Harrison T. Young, Cameron J. Hohimer, Tommaso Proietti, Mo Rastgaar, Cameron J. Hohimer, Came Panagiotis Artemiadis,³ and Conor J. Walsh¹

Abstract

The design of soft actuators is often focused on achieving target trajectories or delivering specific forces and torques, rather than controlling the impedance of the actuator. This article outlines a new soft, tunable pneumatic impedance module based on an antagonistic actuator setup of textile-based pneumatic actuators intended to deliver bidirectional torques about a joint. Through mechanical programming of the actuators (select tuning of geometric parameters), the baseline torque to angle relationship of the module can be tuned. A high bandwidth fluidic controller that can rapidly modulate the pressure at up to 8 Hz in each antagonistic actuator was also developed to enable tunable impedance modulation. This high bandwidth was achieved through the characterization and modeling of the proportional valves used, derivation of a fluidic model, and derivation of control equations. The resulting impedance module was capable of modulating its stiffness from 0 to 100 Nm/rad, at velocities up to 120°/s and emulating asymmetric and nonlinear stiffness profiles, typical in wearable robotic applications.

Keywords: antagonistic actuator, textile-based, pneumatic, fluidic control, tunable stiffness

Introduction

ANY SOFT ROBOTS in the literature are fully deformable, with soft actuators and soft bodies. 1-6 These robots are often prized for their deformability, toughness, and relatively simple manufacturing process.

However, the high deformability of these robots introduces challenges when attempting to exert control over them. In nature, humans and most of the animals eschew some deformability and toughness in favor of control and load capacity, combining compliantly actuated joints with rigid bones.

In a similar way, we can look to combine soft compliant actuators with different rigid mechanisms (joints and linkages), enabling more constrained motion or force application while maintaining the compliance of the systems. $^{7-11}$ These soft actuators have a range of actuation modalities, such as pneumatic, ^{12–15} shape memory alloys, ^{16,17} electroactive polymers ^{18–21} among others. ²² Many of these soft actuators are unidirectional, relying on passive antagonists to return to an initial state. Often this antagonist is simply their structure which undergoes elastic deformation during actuation. 14,18,23-25 Other actuators make use of external antagonists such as gravity²⁶ or thermal effects. ^{16,27}

¹John A. Paulson School of Engineering and Applied Sciences, Harvard University, Cambridge, Massachusetts, USA.

²Polytechnic Institute, Purdue University, West Lafayette, Indiana, USA.
³Department of Mechanical Engineering, College of Engineering, University of Delaware, Newark, Delaware, USA.

Active antagonists can be used for improved controllability and to ensure that the system can be driven to a desired state. 28–30 This strategy mimics the architecture of many human and animal joints, whereby pairs of antagonistic skeletal muscles work together to position and apply torques about a joint. Active antagonists also avoid the need to overcome the static torque of a passive antagonist, allowing smaller actuators to deliver the same output torque. Moreover, with an active antagonistic setup, it is possible to modulate the compliance of the joint, which is desirable for some applications, and, by disabling the actuators, it is possible to achieve full mechanical transparency about the joint.

At the macro scale (1 cm–1 m), inflatable soft actuators are of interest for these antagonistic setups due to their favorable energy density, stroke length, and bandwidth.²² When pneumatically actuated, the compressibility of the air gives these actuators an inherent compliance that can be further tuned through the structure of the actuator.^{31–33} The use of air as a working fluid can also enable remote actuation, allowing for locally lightweight actuation as the controller and fluidic supply can be located away from the actuator in a less mass sensitive location.^{34,35} Textile-based soft actuators^{36–39} can be lighter than their elastomeric counterparts, which can further reduce the weight of the system. Much of the research focus on inflatable soft actuators to date has been focused on achieving certain motions,^{24,40,41} or target forces, but less effort has been placed on dynamically controlling their compliance/impedance.^{42–44}

With traditional electromechanical actuators, compliance can be achieved virtually by implementing high-bandwidth active impedance controllers to accurately modulate the position and force of the actuator to mimic the desired impedance. To modulate the impedance of inherently compliant soft pneumatic actuators, the internal pressure of the inflatable actuators must be rapidly modulated in response to disturbances to the setup. For biomimetic applications such as wearable devices, multi-Hz modulation is required.

Pressure modulation for inflatable soft actuators is commonly achieved using simple binary (on-off) valves, which open and close rapidly to incrementally inflate and deflate the actuators using bang-bang controllers. ^{48,49} These binary

valves must be sized appropriately to ensure adequate pressure resolution as the minimum on time of the valves results in a finite, minimum quantity of fluid transferred in or out of the actuator per on–off cycle. This has the effect of limiting the fidelity of achievable pressure control (Fig. 1). A hysteresis band is typically used to prevent the binary controller continuously oscillating around the set point. For pseudostatic pressure commands, binary valves can achieve low-pressure errors, but when tracking dynamic pressure commands, binary valves can be bandwidth limited (typically $0.1-1\,\mathrm{Hz}^{25,50}$ for soft fluidic actuators) and therefore achieve poorer tracking accuracy, making them less suitable for impedance control.

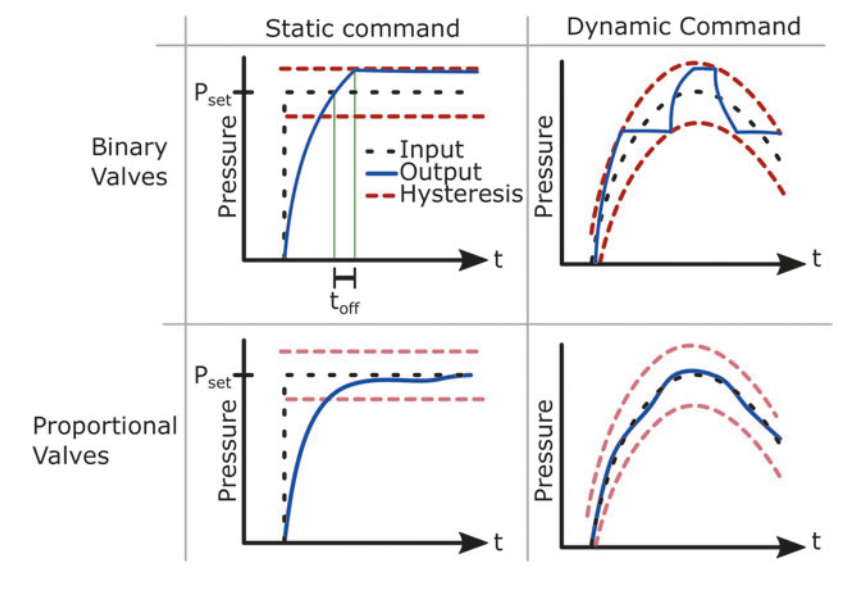
Continuous control over the flow in and out of the actuator is desirable, and the control performance can be improved using proportional valves. Proportional valves are commonly used in hydraulic applications^{51,52} but are yet to see widespread adoption in the literature for pneumatic applications. ^{53,54} By continuously modulating the fluid flow in and out of an actuator, proportional valves achieve much greater pressure fidelity than what can be achieved with similarly sized binary valves. However, the drive requirements for proportional valves are more complicated than binary valves, requiring a proportional voltage or current to modulate the flow, rather than the simple on–off signal to drive a binary valve. Furthermore, the flow output of the proportional valves can be nonlinear. The implementation of a valve model to compensate for this nonlinearity may be necessary to achieve faster and more accurate flow control.

The generalized impedance module and controllers developed in this work may be applied to wearable and soft robotic applications where inherent compliance is desired within certain degrees of freedom.

In this work we:

- Demonstrate the first antagonistic configuration of textilebased pneumatic actuators to deliver bidirectional torque about a joint.
- Demonstrate that using proportional valves we can create a high bandwidth (i.e., multi-Hz pressure trajectories) low-level controller (LLC) to modulate actuator

FIG. 1. Controllers using binary valves must have adequate hysteresis bounds to compensate for their finite on–off time, which can lead to limited tracking accuracy for dynamic profiles. t_{off} is the finite time taken for the valve to close once current is removed. Proportional valves have a variable flow coefficient, thus can finely control the quantity of fluid conveyed. This enables better tracking accuracy for both static and dynamic profiles.



pressure more rapidly and accurately compared to a more commonly employed binary controller (typically 0.1–1 Hz^{25,50} for soft fluidic actuators).

• Present a high-level controller (HLC) to combine both elements to create an impedance module with tunable stiffness and passive damping, and evaluate the ability of the module to emulate the stiffness properties of a biological ankle in the inversion/eversion plane.

The biological impedance of the ankle is critically important for stability when walking, particularly in the inversion/eversion axis, and imitating this biological impedance is a current area of research for ankle prostheses. Sesarch shas shown that this biological impedance varies significantly throughout the gait cycle and with different joint actions (walking, turning, cutting, etc.); thus, the dynamic modulation of a prosthesis impedance is of great interest for improving stability and gait quality. Before any potential integration into a worn prosthetic, the core engineering of this new impedance module design must be first evaluated on the benchtop to determine if it is indeed capable of delivering high stiffness ($\approx 100-120$ Nm/rad) at walking speeds (120 steps/min ≈ 2 Hz) to mimic the biological impedance in the inversion/eversion axis of a healthy ankle.

System Theory

Actuator design

To emulate the biological ankle joint in both stiffness and range of motion (ROM), ^{59,60} the actuators were designed and sized based on our prior work.³⁶ Due to the size constraints of an ankle prosthesis, a shorter but wider actuator design was chosen (Fig. 2) compared to prior work which used longer slender actuators; this form factor yields actuators with a more linear, and thus more desirable, torque to angle response that scales linearly with pressure. Thus, by tuning the actuators geometry and placement, it is possible to "mechanically program" these curves to have desirable impedance properties such as a linear stiffness response when deformed. This in turn can reduce the flow requirements on the fluidic supply, increasing its achievable bandwidth. In this work, a linear torque to angle response was desired as this is equivalent to constant angular stiffness, which potentially allows for a linear relationship between actuator pressure and stiffness. Further details on the design of these actuators can be found in O'Neill et al.³⁶

The torque generated by an actuator τ_x varies linearly with pressure; thus, the actuator torque can be defined as the product of the pressure and a normalized torque to angle function $[f_x(\theta)]$.

$$\tau_x = P_x f_x(\theta) \tag{1}$$

This torque to angle relationship $f_x(\theta)$, and its hysteresis, can be characterized experimentally as shown in Section S1 of the Supplementary Data.

A pair of these actuators (denoted *a*, *b*) can be combined in an antagonistic configuration to deliver bidirectional torques about a joint (Fig. 2). The sum of the actuator torques is the net torque.

$$t_{net} = -P_a f_a(\theta) + P_b f_b(\theta) \tag{2}$$

Controller architecture

The controller developed in this work is broken into a HLC, which generates the appropriate pressure commands for the actuators to achieve the desired impedance, and a LLC to transform the pressure command of the HLC into a current command for the valves in each pressure channel (Fig. 3). The HLC calculates the pressure commands based on the characterized torque response of the actuators as there is no torque sensing in the impedance module design; thus, the HLC must operate in an open loop manner.

Due to the dynamic nature of the proposed application, in this work we developed a fluidic model-based controller to achieve the desired controller bandwidth. To account for the nonlinear flow response of the proportional valves a valve model was also developed for use in the LLC.

Low level pressure controller

Fluidic model. The fluidic model outputs a desired airflow that needs to be achieved to follow the pressure set point. Given the ideal gas law (PV=nRT), the change in gas mass (Δn) associated with an isothermal change $(T=\operatorname{const})$ in pressure (P) and volume (V) can be calculated (Eq. 3). This process is assumed to occur isothermally due to the low operational pressures involved and large effective surface area of the actuators. Note that all pressures are absolute, not gauge pressure, and SI units are used throughout.

$$\Delta n = \frac{P_{set}V_{set} - P_{meas}V_{meas}}{RT} \tag{3}$$

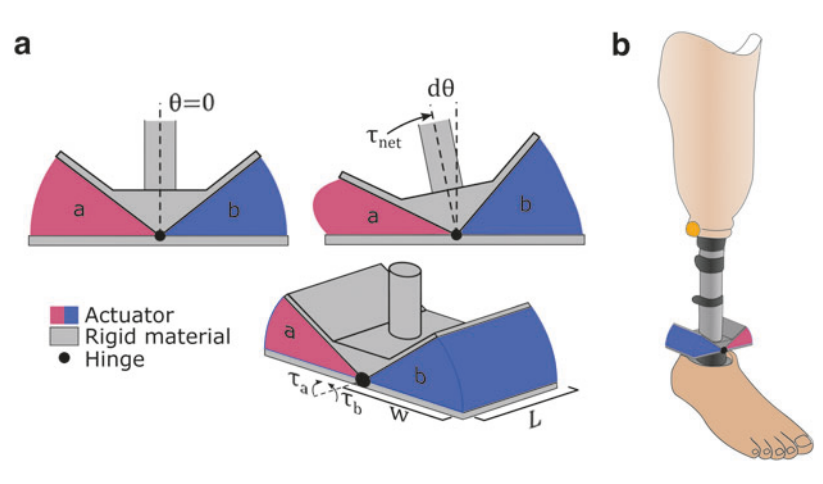


FIG. 2. (a) Antagonistic actuator setup combining two textile-based actuators about a common axis. The *red* "a" actuator is compressed from its equilibrium $(\theta=0)$ by $d\theta$, while the "b" actuator is rarefied by $d\theta$. (b) Concept drawing of how the actuator setup could fit within a prosthetic leg to provide stability in the inversion/eversion during walking.

FIG. 3. Controller breakdown. The HLC determines the required actuator pressure to achieve the desired impedance. The pressure command is passed to the low-level pressure controller which determines the appropriate current to command for the valves. The low-level pressure controller contains the feedforward and feedback fluidic models (Eqs. 6 and 7) and the valve model (Eq. 8). Feedback from the actuator and test rig are used to close the control loop. HLC, high-level controller.

The volume V_x of an actuator x varies as a function of current angle (θ) and pressure (P_x) , but due to the use of inextensible textiles, its pressure sensitivity is very low.³⁶

$$V_{x}(\theta) = f(\theta, P_{x}) \sim f(\theta) \tag{4}$$

The upstream density of a gas is defined as follows:

$$\rho_{upstream,x} = \frac{P_x}{RT} \tag{5}$$

Combining (3–5), the desired flow for a given time step (Q=V/dt) can be calculated for the feedback model, where dt represents the sampling time of the controller:

$$Q_{desired,x} = \begin{cases} \frac{V_{x}(\theta)^{\frac{P_{set,x} - P_{meas,x}}{dt}}}{P_{supply}} & P_{Set} > P_{meas} \text{ (Filling)} \\ \frac{V_{x}(\theta)^{\frac{P_{set,x} - P_{meas,x}}{dt}}}{P_{meas,x}} & P_{set} < P_{meas} \text{ (Venting)} \end{cases}$$
(6)

While filling, the pressure for the upstream density is the supply pressure P_{supply} , while when venting the upstream pressure is that of the actuator $P_{meas,x}$. This results in the system being vent limited, as the supply pressure is inherently greater than the actuator pressure, and remains pseudo constant during filling, unlike the actuator pressure which decreases when exhausting.

The trajectory of P_{set} (estimated as its derivative with respect to time) can also be used to create a feedforward model:

$$Q_{desired,x} = \begin{cases} \frac{V_x(\theta) \binom{dP_{set,x}}{dt}}{P_{supply}} & P_{Set} > P_{meas} \ (Filling) \\ \frac{V_x(\theta) \binom{dP_{set,x}}{dt}}{P_{meas,x}} & P_{set} < P_{meas} \ (Venting) \end{cases}$$
(7)

It is important to note that these volumetric flow rates are dependent on the given upstream density (Eq. 5) for each case (filling of venting). Alternatively, the final fluidic model can be written in terms of mass flow rate, which due to its pressure independence is identical for filling and venting cases:

$$\dot{m}_{desired} = \frac{V_x(\theta)}{RT} \left(\frac{(P_{set,x} - P_{meas,x})}{dt} + \frac{dP_{set,x}}{dt} \right)$$
 (8)

To deliver the calculated flow, a model of the valve is required.

Valve model. The valve model calculates the required current to achieve the desired volumetric flow rate for a given differential pressure across the valve. As the valve is inherently at the specific pressure of the calculated volumetric flow rates, the derived volumetric flow valve model is independent of any upstream pressure, relying only upon the differential pressure across the valve. This is beneficial as the method of valve modeling and characterization natively uses volumetric flow. The following valve model was derived based on the experimentally characterized behavior of the valves (Fig. 4a):

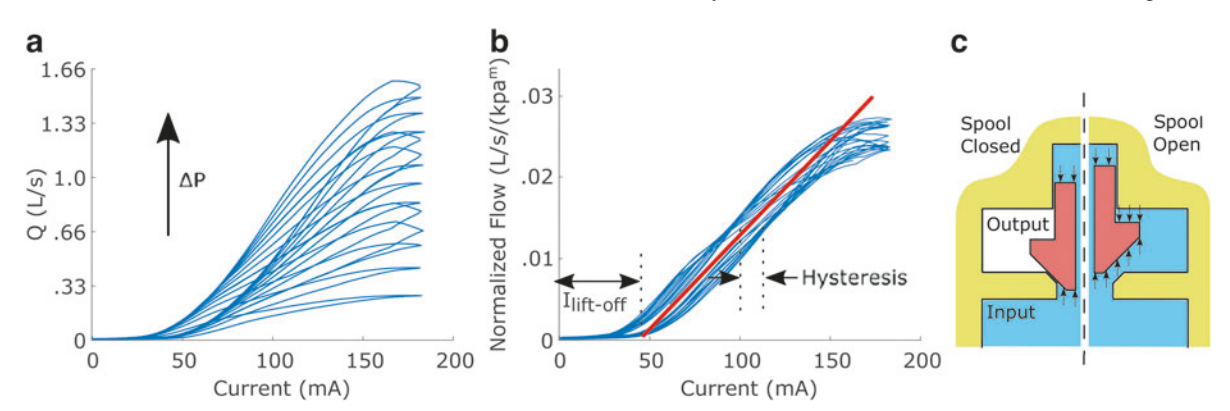


FIG. 4. (a) Characterized flow response of the proportional valves under increasing differential pressure. (b) Normalized flow response of the valve showing the current offset and the linear fit on the mean flow in *red*. (c) When the spool is closed, the forces acting on the spool are balanced due to the pressurization of the upper chamber by the hollow spool. When the spool opens, the forces remain balanced.

$$I_{com} = I_{lift-off} + \frac{\left(\frac{Q_{desired}}{\left(\Delta P_{effective}\right)^{m}} - c_{1}\right)}{c_{2}}$$
(9)

Where the model parameters m, c_I , c_2 , and $I_{lift-off}$ are experimentally determined.

The model normalizes the characterized volumetric flow response of the valves with respect to the power m of the differential pressure (Fig. 4b). The normalized flow response is then approximated by a linear fit with parameters c_1 and c_2 . Due to the balanced spool design of the valves (Fig. 4c), the current in the valve coil need only overcome the preload spring acting on the spool, resulting in a constant liftoff current ($I_{lift-off}$) which acts as a model offset.

Full derivation of the valve model, including hysteresis and behavior under choked flow, as well as the experimental characterization and validation of the valve model, is presented in Section S2 of the Supplementary Data.

High level impedance control

The HLC determines the required pressure for each of the textile-based pneumatic actuators by calculating the necessary resulting torque for a desired impedance. The generalized equation is as follows:

$$\tau_{resulting} = K_{desired}\theta_{error} + d_{desired}\omega_{error} \tag{10}$$

Where $K_{desired}$ and $d_{desired}$ are the desired stiffness and damping, and θ_{error} and ω_{error} are the current angular position error and angular velocity errors, respectively. The torque contribution due to damping is significantly less compared with the stiffness contribution for a biological ankle in the inversion/eversion plane during walking as shown by Ribeiro et al. ⁵⁹ In that study, the average damping in the inversion eversion plane of the ankle was measured at 0.77 ± 27 Nm/rads compared to a stiffness of 66 ± 33 Nm/rad, while peak velocity and displacement were ~ 1.74 rad/s and ~ 0.3 rad, respectively. ^{60,61} As a result, damping is not included in subsequent derivations.

The characteristic equation for the HLC can be derived by equating the net torque from Equation 2 and the resulting torque from Equation 10:

$$-P_{a}f_{a}(\theta) + P_{b}f_{b}(\theta) = K_{desired}\theta_{error}$$
 (11)

To control the equilibrium angle and minimize the effects of the actuator hysteresis, a second characteristic equation is required to solve for a unique pressure for each actuator. By independently controlling the pressure in both actuators, the equilibrium angle can be adjusted by balancing the torques at the desired angle (Fig. 5). As the inherent stiffness of the joint is of interest, an equation relating the stiffness of each actuator to the total joint stiffness is desirable to ensure that inherent system stiffness is equal to the desired stiffness. We can do this by viewing the actuators as two springs in antiparallel, thus the sum of their stiffnesses is the overall system stiffness:

$$P_a K_a(\theta) + P_b K_b(\theta) = K_{desired} \tag{12}$$

Where:

$$K_x(\theta) = \frac{df_x(\theta)}{d\theta} \tag{13}$$

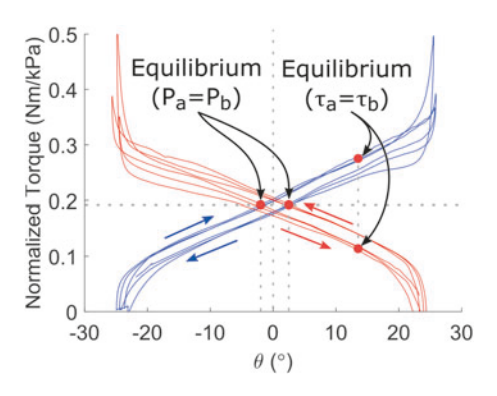


FIG. 5. Torque response curves of the a (*red*) and b (*blue*) actuators. With independent pressure control of the actuators, equilibrium can be achieved by equating pressures or by balancing the torques at a different angle. The direction the setup approaches the equilibrium point determine which hysteresis curve must be followed. The arrows indicate the direction of motion and thus which hysteresis curve is followed.

Full derivation of (12) is presented in Section S3 of the Supplementary Data.

$$P_{a} = \frac{K_{desired}\theta_{error}K_{b}(\theta) + K_{desired}f_{b}(\theta)}{f_{b}(\theta)K_{a}(\theta) - f_{a}(\theta)K_{b}(\theta)}$$
(14)

$$P_{b} = \frac{K_{desired}\theta_{error}K_{a}(\theta) + K_{desired}f_{a}(\theta)}{f_{b}(\theta)K_{a}(\theta) - f_{a}(\theta)K_{b}(\theta)}$$
(15)

Combining and solving for (11 and 12), the unique pressure for each actuator can be calculated.

The actuator specific responses $[K_x(\theta)]$ and $f_x(\theta)$ in these equations are readily obtainable through the experimental characterization of the actuators. As this controller relies on direct modulation of the internal pressure of the individual actuators to achieve the desired impedance, the finite flow through the valves limits the systems bandwidth.

Experimental Setup and Methods

Actuator hardware

The characterization and evaluation in this work were all performed using the previously described benchtop torque rig. ³⁶ A new fixture plate was designed and fabricated to couple the antagonistic actuators to the existing hardware (Fig. 6a). The lower fixture plate was modified to allow the air supply tubes to pass through it, preventing the tubes becoming trapped by the upper fixture plate under large deflection and introducing an error to the torque measurements. A 14-bit encoder (AS5048B; ams AG, Austria) was also retrofitted to the rig for improved angular resolution.

The actuator geometry in this setup is shown in Table 1:

These dimensions were selected based on the expected maximum required net torque, as calculated from the desired impedance and ROM. To reduce the likelihood of the impedance module colliding with the opposite ankle during straight walking, the overall module width was limited to the overall width of a common orthopedic walking boot

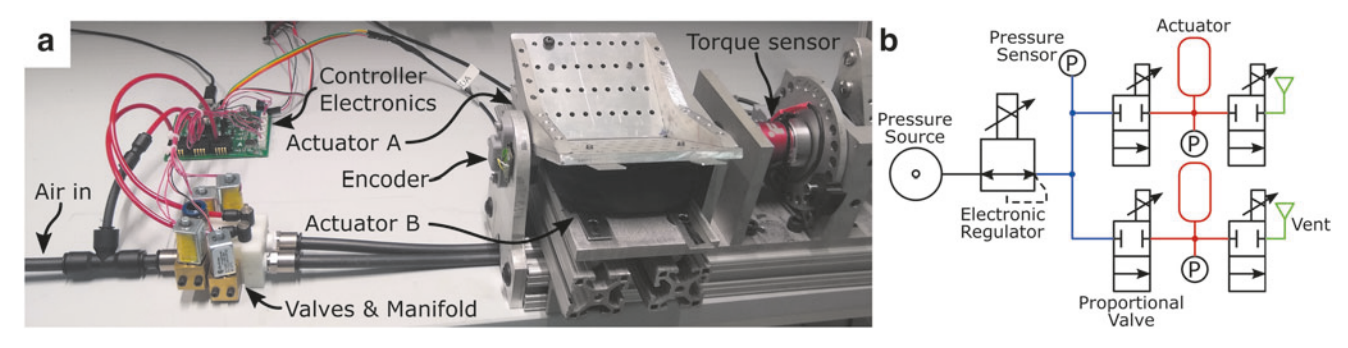


FIG. 6. (a) Benchtop setup for actuator and HLC characterization. The controller electronics contains the pressure sensors and the valve drivers. (b) Pneumatic schematic of the experimental setup and manifold.

(~118 mm, size L DonJoy MaxTrax Walking boot; DJO, USA), resulting in an individual actuator width of 60 mm.

Actuator volume was characterized as a function of angle and pressure by placing the torque rig on a laboratory scale (MS12001L; Mettler Toledo, USA) and injecting water into the actuator while measuring the system mass, pressure, and actuator angle. Details regarding the volume characterization of the actuators can be found in Section S1 of the Supplementary Data.

Pneumatic hardware

Four proportional valves (Polaris; IQ Valves, USA) were mounted on a custom acetal manifold, with push-to-connect ports for all external connections, including actuator pressure measurement near the actuator connectors on the manifold (Fig. 6). This manifold was supplied air by a regulator (AR30-N03E-Z-B; SMC, Japan) fed by the building air supply. The LLC for the valves was run at 250 Hz.

During valve characterization, a flow mass sensor (D6F50A6000; Omron, Japan) was installed in lieu of an actuator to measure the fill flow rate through the valve and manifold assembly. This sensor had a settling time of 150 ms, thus was not suitable for high bandwidth closed loop flow control. Details on the electronics hardware can be found in Section S4 of the Supplementary Data.

The manifold assembly was used for the duration of the study to ensure that any changes in measured flow rate were a result of controller variations, not hardware variations. Thus, for the binary controller, the proportional valves were simply driven between zero and maximum current when appropriate to emulate the on–off behavior of binary valves. Further details on the binary controller can be found in Section S5 of the Supplementary Data.

LLC Characterization

The LLC was experimentally characterized to evaluate its performance before integration with the antagonistic actuator

Table 1. Actuator Geometric Parameters

Length (mm)	Width (mm)	Pattern angle
80	60	60°

Pattern angle refers to the maximum range of motion of the actuator.

setup. For this characterization, the valves and manifold were connected to fixed volume metal containers (275 and 1000 mL; Twistee Cans, USA). These containers were used in place of the textile-based actuators to minimize the effects of internal pressure on internal volume, fully decoupling actuator effects from the LLC characterization. Two volumes were selected to assess the controller over a range of possible actuator sizes, both for this work and others.

The fluidic model can automatically adjust to the current actuator volume, which is highly desirable to ensure stable control of the system. This is particularly important for the actuators of the antagonistic setup whose volume varies significantly when disturbed from equilibrium (Section S1 in the Supplementary Data). This avoids needing to create a gain scheduler and manually tune a proportional-integral (PI) or similar controller over a range of actuator volumes. A binary controller was also evaluated for comparative purposes.

To characterize the bandwidth of the system (defined as magnitude greater than -3 dB), two sinusoidal pressure sweeps were commanded, from 0.1 to 10 Hz (19 discrete frequencies), with a peak-to-peak amplitude of 33 kPa. A bias of 16.5 or 83 kPa was applied to the signal to create the two different sweeps. This resulted in one sweep varying pressure from 0 to 33 kPa, the other from 67 to 100 kPa. The bias pressure is equal to the average actuator pressure throughout the pressure sweep, so two bias pressures were selected to verify the effect of actuator pressure on venting (based on Eq. 6). Each frequency sinusoid was commanded five times before increasing to the next frequency. Supply pressure was set at 270 kPa throughout, which is the supply pressure used on our previous works.

As shown in Figure 7, each controller could achieve the minimum 2 Hz bandwidth design requirement for the smaller volume, with fluidic model controllers achieving significantly higher bandwidth than the binary controller.

With the larger volume actuator, the fluidic model controller again outperforms the binary controller, but still fails to meet the design requirements under the 16.5 kPa bias condition. This result was expected as the bandwidth of each controller is typically vent limited, as predicted by Equation 6. During venting, the pressure differential is limited by the current actuator pressure, which also decreases as the actuator continues to vent. Increasing the bias pressure increased the differential pressure available for venting of the actuator, in turn increasing the bandwidth of the LLC.

When the phase response of this characterization is broken into a fill phase delay and vent phase delay, this vent limiting

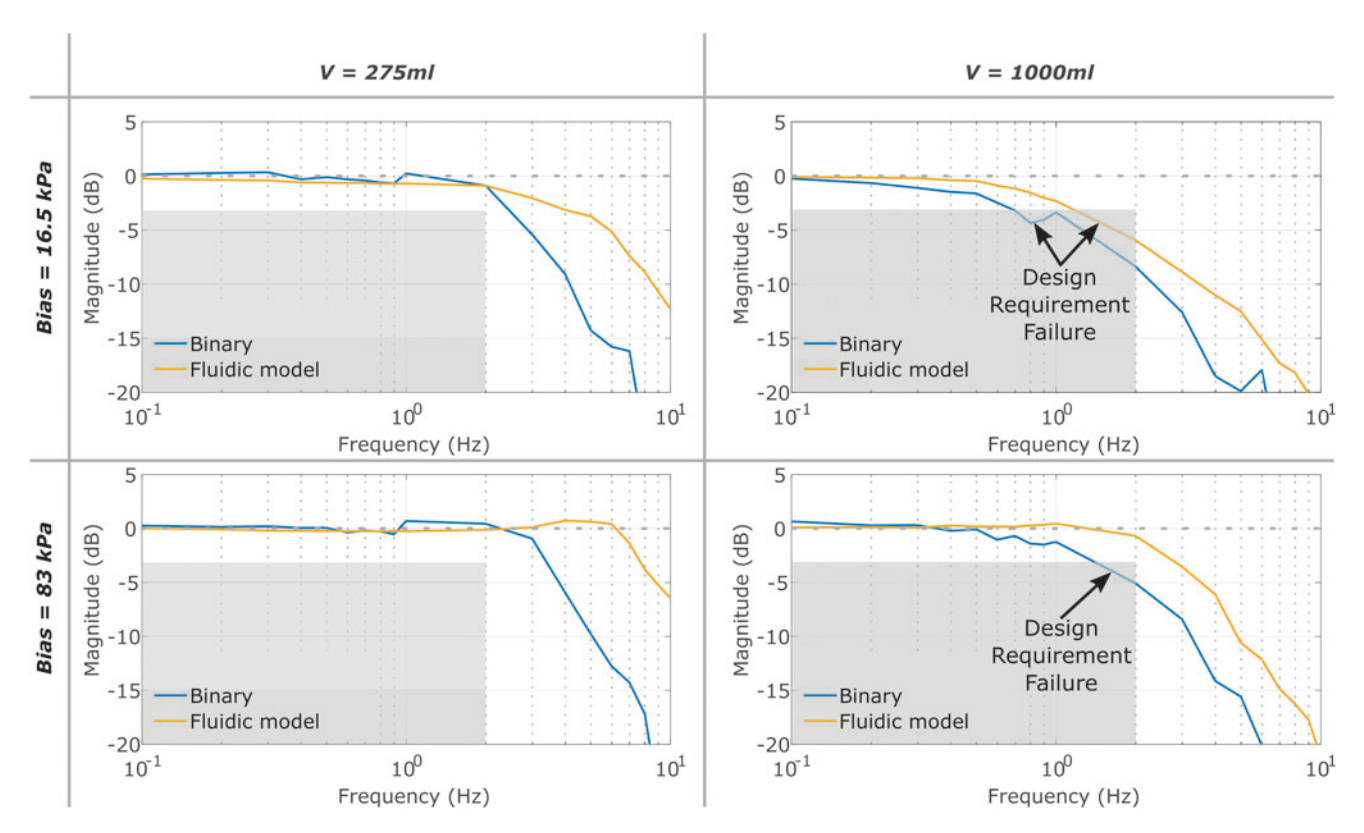


FIG. 7. Frequency response of the evaluated controllers as functions of volume and bias pressure. Intersection with the shaded area represents a failure to meet the 2 Hz minimum bandwidth.

is readily apparent. In Figure 8a, the best and worst-case scenarios (high bias pressure and small volume vs low bias pressure and large volume, respectively) are contrasted to illustrate how the system is vent limited. In the worst-case scenario, we observed approximately -90° of phase lag experienced by the fluidic model control at the target bandwidth of 2 Hz. However, under the best-case condition (expected prosthetic use condition), a similar vent phase lag only occurs above 6 Hz.

Reductions in supply pressure do result in decreased bandwidth (Fig. 8b); however, once the supply pressure was

more than \sim 66 kPa above the actuator pressure (Fig. 8b, P_{supply} = 166 kPa, yellow), further increases in pressure had limited effect.

Impedance Implementation

The HLC is the final component of the impedance module, and its performance directly affects the overall performance. To evaluate the HLCs ability to modulate the stiffness of the impedance module, a pseudo-static stiffness characterization was performed over a range of desired stiffnesses (25–100).

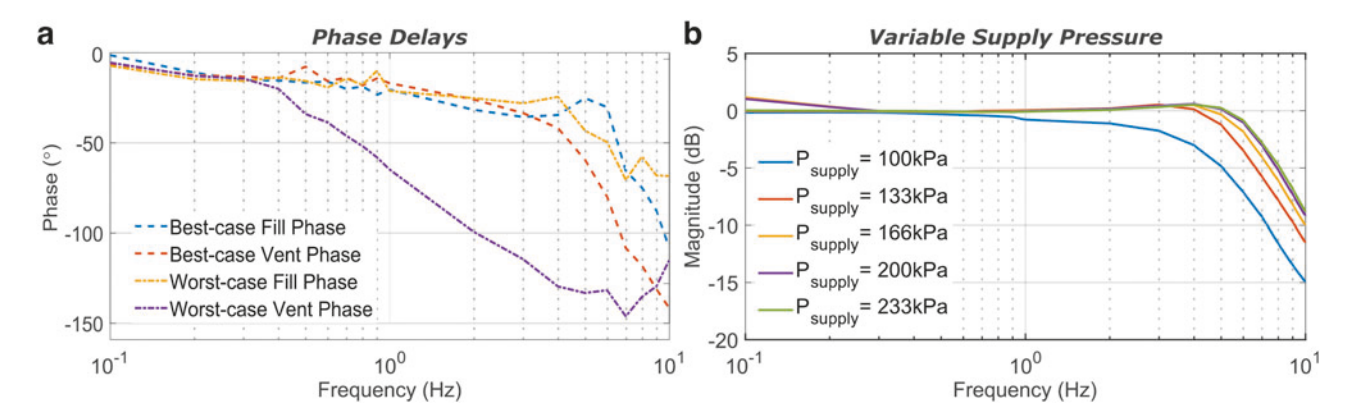
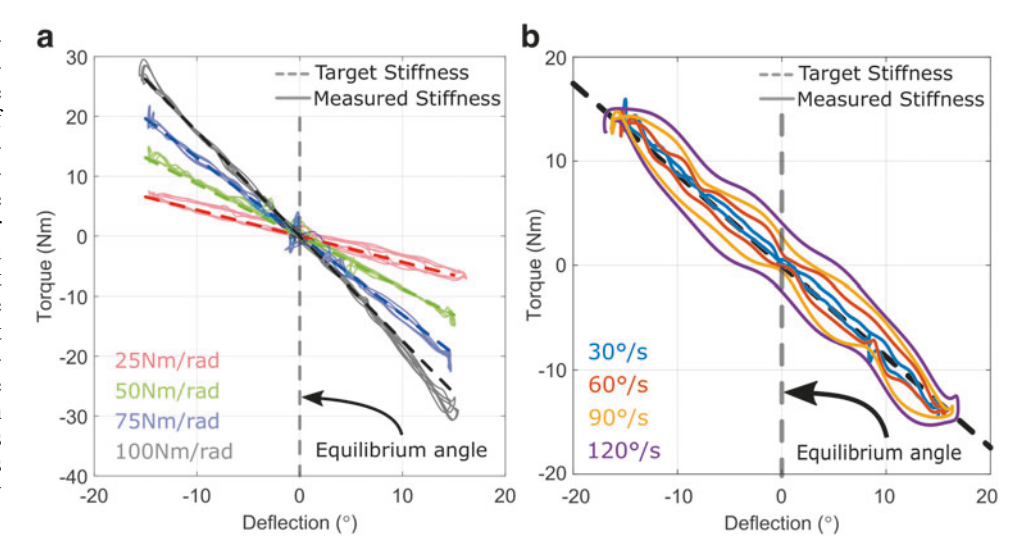


FIG. 8. (a) Fill and vent phase delay for both best case (high bias pressure and small volume) and worst case (low bias pressure, high volume) conditions. Vent phase delay is most pronounced in the worst case scenario due to the low bias pressure, while the worst case fill phase delay is virtually identical to the best case fill phase delay. (b) Effect of supply pressure on the low-level controller bandwidth with the small volume actuator. Peak actuator pressure was 100 kPa.

FIG. 9. (a) The independently pressurized HLC accurately modulates the torque output across the range of deflections and target stiffnesses. (b) Dynamic response of the impedance module at various angular velocities with the dashed line representing the target stiffness of 50 Nm/rad. The 30°/s response is equivalent to the pseudo-static condition. The HLC maintains the desired stiffness at these high velocities; however, it does develop a notable hysteresis that increases as velocity increases.



Nm/rad in steps of 25 Nm/rad). The setup was deflected from rest ($\approx 0^{\circ}$) to $\pm 15^{\circ}$ thrice at constant velocity ($\approx 30^{\circ}$ /s), while the net torque was measured by the benchtop test rig. This velocity correlated with moving from one deflection limit to the opposite deflection limit in 1s. The results of this characterization for the HLC are shown in Figure 9a.

The HLC demonstrates good linearity and ability to track the applied deflection and apply the appropriate net torque to achieve the desired impedance (dashed lines), achieving a normalized stiffness error of $6.9\pm1.7\%$ across the range of evaluated stiffnesses and deflections. Based on the actuator characterization of Figure 5 and our previous work, ³⁶ we expect nonlinear behavior as either actuator approaches full compression (final $5-10^\circ$) of motion due to the parallel stiffness contribution of the bunched up textile.

In practice, the impedance module is expected to be subjected to dynamic disturbances, and the HLC must react rapidly to appropriately modulate the system impedance. To characterize the dynamic response of the system, a $\pm 15^{\circ}$ angular disturbance was applied to the setup with velocity sweeping from 30°s to 120°/s while the HLC was commanded to maintain a stiffness of 50 Nm/rad. The results of this characterization can be seen in Figure 9b.

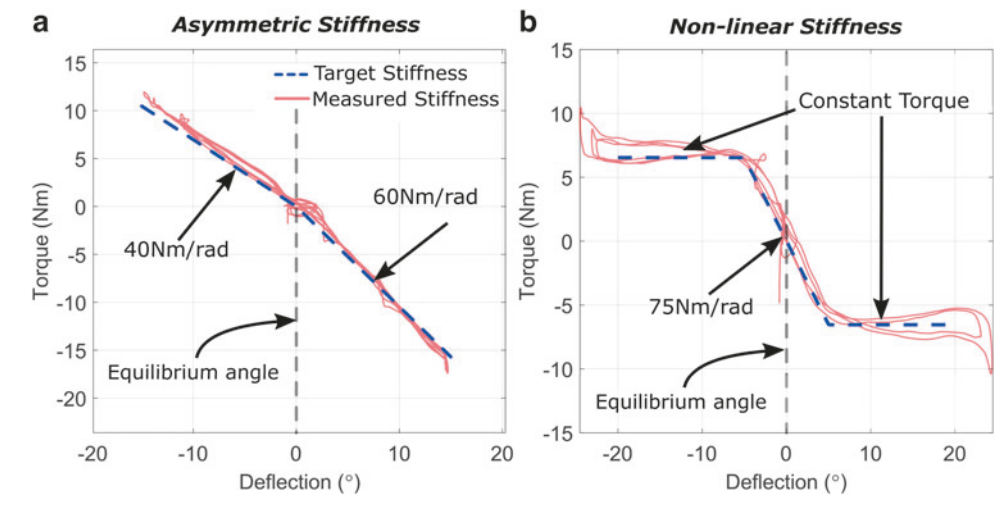
The observed torque error from the desired response is the result of increasing pressure modulation error. This is caused

by fundamental limitations of the systems, namely the compressibility of fluids introducing delays in sensing rapid changes in pressure, and the finite bandwidth of the LLC and the proportional valves. When the module is disturbed, one actuator becomes compressed, increasing its pressure, while the other actuator becomes rarefied, decreasing its pressure. The inherent propagation delay in sensing this pressure change and responding accordingly results in greater net torque being applied by the actuator pair than desired, resulting in the observed hysteresis.

The effect of this lag becomes more pronounced at higher velocities as there is a greater error between the measured and instantaneous pressures. This results in the correct magnitude stiffness being applied (correct slope) but with a torque offset due to the sensing lag. The magnitude of this torque hysteresis was characterized as 0.032 Nm/°/s, which is the passive damping coefficient of the module. We were unable to complete the velocity sweep with a desired stiffness of 100 Nm/rad due to persistent failure of the actuators from overpressure at the higher velocities (90°/s and 120°/s). These conditions represented the limits of both velocity and stiffness of the system, with the module absorbing $\sim 110~{\rm W}$ continuously during testing.

Considering the future application of assisting walking, a controller should be able to reduce this hysteresis by

FIG. 10. (a) Angle based asymmetric stiffness with a 40 Nm/rad stiffness for negative deflections and a 60 Nm/rad stiffness for positive deflections. (b) Piecewise constant torque demonstration. For deflections greater than ±5°, the stiffness is modulated to maintain a constant torque output, while for deflection less than ±5°, a stiffness of 75 Nm/rad was commanded.



observing where in the gait cycle the wearer is and preemptively venting the compressed actuator when loading is expected based on the gait mechanics. In future work, we will aim to confirm this hypothesis and if this will prevent the observed failures under high stiffness and speed.

To demonstrate the flexibility of the impedance module and the HLC in this work, asymmetric and nonlinear profiles were also implemented, as shown in Supplementary Video S1. Asymmetric stiffnesses, which are common in biological joints such as the ankle during dorsiflexion/plantar flexion, ⁵⁹ can be configured to be angle dependent (Fig. 10a) or velocity dependent, whereby the systems are stiffer in one direction than the other.

Arbitrary nonlinear stiffnesses can also be achieved such as the piece-wise constant torque response shown in Figure 10b. The ability of this system to dynamically modulate its impedance on command is very powerful and may enable the use of such an impedance module in a wide variety of applications.

Conclusion and Future Work

A tunable textile-based impedance module is presented and validated in this work. Under pseudo-static conditions, the impedance module was capable of open-loop stiffness tuning from 0 Nm/rad to in excess of 100 Nm/rad with a normalized error of $6.9\pm1.7\%$, while controllable stiffness could be maintained at angular velocities of up to 120° /s. These figures match those described in the literature for stiffness and velocity in the inversion eversion plane of the ankle during walking [66 ± 33 Nm/rad and ~1.74 rad/s (100° /s)]. The module has a passive damping coefficient of 0.032 Nm/rad/s and the potential to directly modulate damping in future work.

The module is also capable of implementing asymmetric and nonlinear stiffness profiles on command. The module used an antagonistic arrangement of textile based unfolding actuators for bidirectional torque control, coupled with proportional valves for high bandwidth continuous flow control of the actuators. Low-level pressure control was achieved using a fluidic model of the actuators and valves, while HLC was used to determine the required actuator pressures to achieve the desired impedance. The fluidic model developed in this work allows the LLC to automatically adjust to the varying volume of the actuator, avoiding the need for gain scheduler based on manual tuning across a range of actuator volumes.

The main limitation of the developed impedance module is its dynamic response. While the response remains linear and tracks the correct stiffness value, a minor torque hysteresis which scales with angular velocity is introduced. This introduces a torque offset which uncontrollably alters the equilibrium angle of the module. To further improve the dynamic response of the module and reduce this torque hysteresis, flow restriction in the flow path must be reduced, in addition to implementation of higher speed valves. Assisted venting of the system, such as a vacuum applied to the vent exhaust to increase the differential pressure during venting, may also be required.

To conclude, this work provides a foundation for future development of hybrid impedance modules combining rigid structures with soft compliant actuation. In particular, this work is the first step in the development of an ankle impedance module to assist with ankle stability during level-ground walking by amputees, although the fluidic supply and controllers developed during this work can be used in a range of other soft robotic applications.

Author Disclosure Statement

The authors declare no known conflicts of interest.

Funding Information

This work was supported by the National Science Foundation (NRI Grant No. 2025797) and the Harvard John A. Paulson School of Engineering and Applied Sciences.

Supplementary Material

Supplementary Data Supplementary Video S1

References

- 1. Tolley MT, Shepherd RF, Mosadegh B, et al. A resilient, untethered soft robot. Soft Robot 2014;1(3):213–223.
- Onal CD, Chen X, Whitesides GM, et al. Soft mobile robots with on-board chemical pressure generation. Springer Tracts Adv Robot 2017;100:525–540.
- 3. Martinez RV, Branch JL, Fish CR, et al. Robotic tentacles with three-dimensional mobility based on flexible elastomers. Adv Mater 2013;25(2):205–212.
- 4. Veale AJ, Xie SQ, Anderson IA. Modeling the peano fluidic muscle and the effects of its material properties on its static and dynamic behavior. Smart Mater Struct 2016; 25(6):065014.
- Calisti M, Picardi G, Laschi C. Fundamentals of soft robot locomotion. J R Soc Interface 2017;14(130):20170101.
- Hawkes EW, Blumenschein LH, Greer JD, et al. A soft robot that navigates its environment through growth. Sci Robot 2017;2(8):3028.
- Stokes AA, Shepherd RF, Morin SA, et al. A hybrid combining hard and soft robots. Soft Robot 2014;1(1):70— 74.
- 8. Rose CG, O'Malley MK. Hybrid rigid-soft hand exoskeleton to assist functional dexterity. IEEE Robot Autom Lett 2019;4(1):73–80.
- 9. Chen Y, Wan F, Wu T, et al. Soft-rigid interaction mechanism towards a lobster-inspired hybrid actuator. J Micromech Microeng 2018;28(1):014007.
- Bartlett NW, Tolley MT, Overvelde JTB, et al. A 3D-printed, functionally graded soft robot powered by combustion. Science (80-.) 2015;349(6244):161–165.
- 11. Kumar K, Liu J, Christianson C, et al. A biologically inspired, functionally graded end effector for soft robotics applications. Soft Robot 2017;4(4):317–323.
- Keiko Ogura, Wakimoto S, Suzumori K, et al. Micro pneumatic curling actuator—Nematode actuator. In: 2008 IEEE International Conference on Robotics and Biomimetics. IEEE; 2009; pp. 462–467.
- 13. Galloway KC, Becker KP, Phillips B, et al. Soft robotic grippers for biological sampling on deep reefs. Soft Robot 2016;3(1):23–33.
- Gorissen B, Reynaerts D, Konishi S, et al. Elastic inflatable actuators for soft robotic applications. Adv Mater 2017; 29(43):1604977.
- 15. Villegas D, Van Damme M, Vanderborght B, et al. Thirdgeneration pleated pneumatic artificial muscles for robotic

- applications: Development and comparison with McKibben Muscle. Adv Robot 2012;26(11–12):1205–1227.
- Gafford J, Aihara H, Thompson C, et al. Distal proprioceptive sensor for motion feedback in endoscope-based modular robotic systems. IEEE Robot Autom Lett 2018; 3(1):171–178.
- 17. Wang Z, Hang G, Li J, et al. A micro-robot fish with embedded SMA wire actuated flexible biomimetic fin. Sens Actuat A Phys 2008;144(2):354–360.
- Gupta U, Qin L, Wang Y, et al. Soft robots based on dielectric elastomer actuators: A review. Smart Mater Struct 2019;28(10):103002.
- Li WB, Zhang WM, Zou HX, et al. A fast rolling soft robot driven by dielectric elastomer. IEEE ASME Trans Mechatron 2018;23(4):1630–1640.
- Duduta M, Berlinger F, Nagpal R, et al. Tunable multimodal locomotion in soft dielectric elastomer robots. IEEE Robot Autom Lett 2020;5(3):3868–3875.
- 21. Shea H, Bing Z, Shintake J, et al. Jellyfish-inspired soft robot driven by fluid electrode dielectric organic robotic actuators. Front Robot AI 2019;6:126.
- 22. Zhang J, Sheng J, O'Neill CT, et al. Robotic artificial muscles: Current progress and future perspectives. IEEE Trans Robot 2019;35(3):761–781.
- 23. Yang D, Verma MS, So J-H, et al. Buckling pneumatic linear actuators inspired by muscle. Adv Mater Technol 2016;1(3):1600055.
- Connolly F, Walsh CJ, Bertoldi K. Automatic design of fiber-reinforced soft actuators for trajectory matching. Proc Natl Acad Sci U S A 2017;114(1):51–56.
- Polygerinos P, Wang Z, Galloway KC, et al. Soft robotic glove for combined assistance and at-home rehabilitation. Rob Auton Syst 2015;73:135–143.
- 26. O'Neill C, Proietti T, Nuckols K, et al. Inflatable soft wearable robot for reducing therapist fatigue during upper extremity rehabilitation in severe stroke. IEEE Robot Autom Lett 2020;5(3):3899–3906.
- 27. Kotikian A, Morales JM, Lu A, et al. Innervated, self-sensing liquid crystal elastomer actuators with closed loop control. Adv Mater 2021;33(27):2101814.
- Baiden D, Ivlev O. Independent torque and stiffness adjustment of a pneumatic direct rotary soft-actuator for adaptable human-robot-interaction. In: 2014 23rd International Conference on Robotics in Alpe-Adria-Danube Region (RAAD). IEEE; 2015; pp. 0–5.
- Niiyama R, Rus D, Kim S. Pouch motors: Printable/ inflatable soft actuators for robotics. In: 2014 IEEE International Conference on Robotics and Automation (ICRA). IEEE; 2014; pp. 6332–6337.
- 30. Kang BB, Choi H, Lee H, et al. Exo-Glove Poly II: A polymer-based soft wearable robot for the hand with a tendon-driven actuation system. Soft Robot 2019;6(2):214–227.
- 31. Cappello L, Galloway KC, Sanan S, et al. Exploiting textile mechanical anisotropy for fabric-based pneumatic actuators. Soft Robot 2018;5(5):662–674.
- 32. Connolly F, Polygerinos P, Walsh CJ, et al. Mechanical programming of soft actuators by varying fiber angle. Soft Robot 2015;2(1):26–32.
- 33. Bishop-Moser J, Kota S. Design and modeling of generalized fiber-reinforced pneumatic soft actuators. IEEE Trans Robot 2015;31(3):536–545.
- 34. Wehner M, Quinlivan B, Aubin PM, et al. A lightweight soft exosuit for gait assistance. In: Proceedings—IEEE

- International Conference on Robotics and Automation. IEEE; 2013; pp. 3362–3369.
- 35. Mooney LM, Herr HM. Biomechanical walking mechanisms underlying the metabolic reduction caused by an autonomous exoskeleton. J Neuroeng Rehabil 2016;13(1):1–12.
- O'Neill CT, McCann CM, Hohimer CJ, et al. Unfolding textile-based pneumatic actuators for wearable applications. Soft Robot 2022;9(1):163–172.
- Simpson C, Huerta B, Sketch S, et al. Upper extremity exomuscle for shoulder abduction support. IEEE Trans Med Robot Bionics 2020;2(3):474–484.
- Nesler CR, Swift TA, Rouse EJ. Initial design and experimental evaluation of a pneumatic interference actuator. Soft Robot 2018;5(2):138–148.
- 39. Fang J, Yuan J, Wang M, et al. Novel accordion-inspired foldable pneumatic actuators for knee assistive devices. Soft Robot 2020;7(1):95–108.
- 40. Nguyen PH, Zhang W. Design and computational modeling of fabric soft pneumatic actuators for wearable assistive devices. Sci Rep 2020;10(1):1–13.
- 41. Rus D, Tolley MT. Design, fabrication and control of soft robots. Nature 2015;521(7553):467–475.
- 42. Narang YS, Vlassak JJ, Howe RD. Mechanically versatile soft machines through laminar jamming. Adv Funct Mater 2018;28(17):1707136.
- 43. Sadeghi A, Mondini A, Mazzolai B. A vacuum powered soft textile-based clutch. Actuators 2019;8(2):47.
- Paoletti P, Jones GW, Mahadevan L. Grasping with a soft glove: Intrinsic impedance control in pneumatic actuators. J R Soc Interface 2017;14(128):20160867.
- 45. Pratt GA, Williamson MM. Series elastic actuators. In: Proceedings 1995 IEEE/RSJ International Conference on Intelligent Robots and Systems. Human Robot Interaction and Cooperative Robots. IEEE; 1995; pp. 1399–1406.
- 46. Haldane DW, Plecnik MM, Yim JK, et al. Robotic vertical jumping agility via series-elastic power modulation. Sci Robot 2016;1(1):eaag2048.
- 47. Vanderborght B, Albu-Schaeffer A, Bicchi A, et al. Variable impedance actuators: A review. Rob Auton Syst 2013; 61(12):1601–1614.
- 48. Verrelst B, Van Ham R, Vanderborght B, et al. The pneumatic biped "Lucy" actuated with pleated pneumatic artificial muscles. Auton Robots 2005;18(2):201–213.
- 49. Polygerinos P, Correll N, Morin SA, et al. Soft robotics: Review of fluid-driven intrinsically soft devices; Manufacturing, sensing, control, and applications in human-robot interaction. Adv Eng Mater 2017;19:1–22.
- 50. Xiloyannis M, Alicea R, Georgarakis A-M, et al. Soft robotic suits: State of the art, core technologies, and open challenges. IEEE Trans Robot 2022;38(3):1343–1362.
- Tamburrano P, Plummer AR, Distaso E, et al. A review of direct drive proportional electrohydraulic spool valves: Industrial state-of-the-art and research advancements. J Dyn Syst Meas Control Trans ASME 2019;141(2):020801.
- 52. Renn JC, Tsai C. Development of an unconventional electro-hydraulic proportional valve with fuzzy-logic controller for hydraulic presses. Int J Adv Manuf Technol 2005;26(1–2):10–16.
- 53. Saravanakumar D, Mohan B, Muthuramalingam T. A review on recent research trends in servo pneumatic positioning systems. Precis Eng 2017;49:481–492.
- 54. Huang H, Wu L, Lin J, et al. A novel mode controllable hybrid valve pressure control method for soft robotic gripper. Int J Adv Robot Syst 2018;15(5):1–12.

- 55. Ficanha EM, Ribeiro GA, Dallali H, et al. Design and preliminary evaluation of a two DOFs cable-driven ankle-foot prosthesis with active dorsiflexion-plantarflexion and inversion-eversion. Front Bioeng Biotechnol 2016;4:36.
- Major MJ, Twiste M, Kenney LPJ, et al. The effects of prosthetic ankle stiffness on stability of gait in people with transtibial amputation. J Rehabil Res Dev 2016;53(6):839– 852.
- 57. Koehler-McNicholas SR, Savvas Slater BC, Koester K, et al. Bimodal ankle-foot prosthesis for enhanced standing stability. PLoS One 2018;13(9):e0204512.
- Au S, Berniker M, Herr H. Powered ankle-foot prosthesis to assist level-ground and stair-descent gaits. Neural Networks 2008;21(4):654–666.
- Ribeiro GA, Knop LN, Rastgaar M. Multi-directional ankle impedance during standing postures. IEEE Trans Neural Syst Rehabil Eng 2020;28(10):2224–2235.

- 60. Brockett CL, Chapman GJ. Biomechanics of the Ankle. Orthop Trauma 2016;30(3):232–238.
- 61. Nester CJ, Jarvis HL, Jones RK, et al. Movement of the human foot in 100 pain free individuals aged 18–45: Implications for understanding normal foot function. J Foot Ankle Res 2014;7(1):51.

E-mail: walsh@seas.harvard.edu